Microfluidic Synthesis of Cobalt Nanoparticles

Yujun Song,[†,‡] Hartwig Modrow,[§] Laurence L. Henry,[||] Cheng K. Saw,[⊥] E. E. Doomes,[†,#] Vadim Palshin,[†] Josef Hormes,[†] and Challa S. S. R. Kumar*[,†]

Center for Advanced Microstructures and Devices, Louisiana State University, 6980 Jefferson Highway, Baton Rouge, Louisiana 70806, Physikalisches Institut, University of Bonn, Nussallee 12, D-53115 Bonn, Germany, Department of Physics, Southern University and A&M College, Baton Rouge, Louisiana 70813, and Lawrence Livermore National Laboratory, Livermore, California 94550

Received December 20, 2005. Revised Manuscript Received February 9, 2006

Co nanoparticles with three different crystal structures were synthesized in a microfluidic reactor through manipulation of reaction times, flow rates, and quenching procedures. Cobalt nanoparticles of face-centered cubic (β) phase were obtained from a high flow rate of the reactants followed by in situ quenching of the reaction. hcp and ϵ-cobalt nanoparticles were obtained at a low flow rate of the reactants followed by in situ quenching and delayed quenching, respectively. The crystal structures were characterized using Co K-edge X-ray absorption near edge structure (XANES) spectroscopy, X-ray diffraction (XRD), and selected area electron diffraction (SAED). In situ XANES measurements on Co nanoparticles coming out of the outlet of the microfluidic reactor at different flow rates seem to indicate that the difference in flow rate influences the nucleation process in a critical way and that particle growth occurs mainly outside the reactor. The magnetic properties of the cobalt nanoparticles, measured using a SQUID magnetometer system, showed significant differences among the samples and are consistent with the three different crystal structures.

1. Introduction

Engineering of nanomaterials is the primary focus of numerous research groups as nanomaterials find extensive industrial applications in the field of catalysis, electronics, high-density magnetic recording media, sensors, nanobiotechnology, and biomedical nanotechnology.[1] Several synthesis methodologies, both "top-down" and "bottom-up" approaches, have been developed to obtain a broad variety of nanomaterials of different sizes and shapes.[2] Among the bottom-up approaches, a wet-chemical approach appears to be most promising for industrial applications because of its intrinsic scale-up potential. Wet-chemical synthesis methods can be broadly classified into co-precipitation and chemical reduction, which can be carried out either in traditional "flask" techniques or microfluidic processes. However, the challenge continues to be the control of the size, size distribution, shape, crystal structure, and surface modifications of the nanoparticles. These different parameters, as it is now well-established, affect both physical and chemical properties such as electrical, optical, magnetic, and biological properties. The key parameters that determine the size of the nanoparticles in wet-chemical synthesis are the ratio of stabilizing surfactant to the precursor salt, chemical nature of the surfactant, and control of reaction kinetics through rapid nucleation followed by growth.[3] In fact, in a very recent report, Park et al. demonstrated synthesis of iron oxide nanoparticles with an accuracy of 1 nm with diameters of 6−13 nm.[4] The shape of the nanomaterials appears to be governed by the shape of the surfactant-based template being utilized, the chemical nature of the capping agents, and quenching procedures.[5,6] In addition to the traditional wet-chemical methods, it was recently demonstrated that microreactors offer a better control of the reaction kinetics parameter than the conventional batch processes as a result

* To whom correspondence should be addressed. E-mail: ckumar1@lsu.edu.
† Louisiana State University.
‡ Current address: Applied Research Centre at Old Dominion University, Newport News, VA 23606.
§ University of Bonn.
|| Department of Physics, Southern University and A&M College.
⊥ Lawrence Livermore National Laboratory.
Current address: Department of Physics, Southern University and A&M College.

(1) (a) Lisiecki, I. *J. Phys. Chem. B* **2005**, *109*, 12231. (b) Green, M. *Chem. Commun.* **2005**, 3002. (c) Liu, Y.; Majetich, S. A.; Tilton, R. D.; Sholl, D. S.; Lowry, G. V. *Environ. Sci. Technol.* **2005**, *39* (5), 1338. (d) Farrell, D.; Cheng, Y.; McCallum, R. W.; Sachan, M.; Majetich, S. A. *J. Phys. Chem. B* **2005**, *109* (28), 13409. (e) Catherine, B. *J. Mater. Chem.* **2005**, *15* (5), 543. (f) Kumar, C. S. S. R., Hormes, J., Leuschner, C., Eds. *Nanofabrication towards biomedical applications*; Wiley-VCH: New York, 2004. (g) Kumar, C. S. S. R., Ed. *Biofunctionalization of nanomaterials*; Wiley-VCH: New York, 2005. (h) Cheng, C.; Romero, D.; Fraser, G. T.; Walker, A. R. H. *Langmuir* **2005**, *21* (26), 12055.

(2) (a) Richards, R. M.; Bönnemann, H. In *Nanofabrication Towards Biomedical Applications: Techniques, Tools, Applications, and Impact*; Kumar, C. S. S. R., Hormes, J., Leuschner, C., Eds.; Wiley-VCH: New York, 2004, pp 3−32. (b) Cushing, B. L.; Kolesnichenko, V. L.; O'Connor, C. J. *Chem. Rev.* **2004**, *104*, 3893.

(3) (a) Popov, A. K.; Brummer, J.; Tanke, R. S.; Taft, G.; Wruck, A.; Loth, M.; Langlois, R.; Schmitz, R. Los Alamos National Laboratory, Preprint Archive, Physics, 2005, 1−15, arXiv:physics/0511147. (b) de Dios, M.; Barroso, F.; Tojo, C.; Blanco, M. C.; Lopez-Quintela, M. A. *Colloids Surf., A* **2005**, *270−271* (Complete), 83−87. (c) Frenkel, A. I.; Nemzer, S.; Pister, I.; Soussan, L.; Harris, T.; Sun, Y.; Rafailovich, M. H. *J. Chem. Phys.* **2005**, *123* (18), 184701/1. (d) Hussain, I.; Graham, S.; Wang, Z.; Tan, B.; Sherrington, D. C.; Rannard, S. P.; Cooper, A. I.; Brust, M. *J. Am. Chem. Soc.* **2005**, *127* (47), 6398.

(4) Park, J.; Lee, E.; Hwang, N.-M.; Kang, M.; Kim, C. S.; Hwang, Y.; Park, J. G.; Noh, H. G.; Kim, J. Y.; Park, J. H.; Hyeon, T. *Angew. Chem., Int. Ed.* **2005**, *44*, 2872.

10.1021/cm052811d CCC: $33.50
Published on Web 05/20/2006

of efficient heat and mass transfer within the microliter reactant volume, and they have been utilized for size-control synthesis of nanoparticles.[7−10] It appears, therefore, that the control of nanoparticle size and shape is almost well-understood.

In contrast to that, there are not many reports of investigations of methods for controlled synthesis of nanoparticles with desired crystal structure. Control of the crystal structure is one of the key issues in nanoparticle synthesis because physical and chemical properties also depend directly on their crystal structures.[11−16] This is of special importance when several crystal structures with small energy differences exist, for example, in the case of cobalt nanoparticles where at least three crystal structures are known. Conventional techniques such as thermal annealing,[12,15] pressure-induced phase transition,[13,16] ball milling,[17] surfactant-induced phase transition,[18,19] and size-dependent phase transition[20] have been explored to obtain nanoparticles of defined crystal structure. However, there is no single synthesis method that provides a possibility to prepare a selected crystal structure of nanoparticles in general and cobalt nanoparticles in particular unless one resorts to significant variation of experimental conditions or other properties.[21,24]

Our group has been involved in the synthesis of metal nanoparticles, more specifically magnetic nanoparticles, using traditional wet-chemical as well as microfludic processes.[10,22] Among the metallic nanoparticles, cobalt is the most well-studied because of its unique properties and potential applications. Cobalt nanoparticles are known to exist in three polymorphs, the face-centered cubic (fcc), hexagonally close packed (hcp), and epsilon (ϵ) phases. All three phases have different magnetic properties. The hcp and fcc phases are known to exist at room temperature, whereas the ϵ phase is considered as a metastable phase. The hcp phase cobalt with anisotropic high magnetic coercivity is more useful for permanent magnetic applications, and the fcc cobalt nanoparticles have soft magnetic properties. The net anisotropy of ϵ nanoparticles is smaller than that of fcc cobalt, which is an order of magnitude smaller than that of hcp cobalt.[23]

A wet-chemical synthetic approach using thermolysis of dicobaltoctacarbonyl by varying the reaction conditions and capping agents is the only known single reaction to provide cobalt nanoparticles of all the three different phases.[1b] It is well-known that the synthesis via solution phase reduction of metal salts is often controlled kinetically rather than thermodynamically, leading to the possibility of obtaining nanoparticles in metastable phases.[24] We report here for the first time a microfluidic process for obtaining all the three phases of cobalt nanoparticles. We hypothesized that kinetic energies of the reactants can be controlled better in a microfludic environment through appropriate design of micromixers and manipulation of flow rates which in turn lead to controlling the crystal structure of the nanoparticles. While microfluidic processes for size and shape controlled synthesis of nanoparticles are known, there is no report of crystal structure controlled synthesis using these approaches.[25] The microfluidic synthesis results reported here, in conjunction with analysis based on selected area electron diffraction (SAED), X-ray diffraction (XRD), and in situ liquid Co K-edge X-ray absorption near edge structure (XANES) spectroscopy, demonstrate that hcp (α), fcc (β), and epsilon (ϵ) crystal structures of cobalt nanoparticles can be obtained by controlling the reaction times, flow rates, and quenching procedures. The effect of the structural changes on the magnetic properties of the particles obtained using SQUID magnetometry is also reported.

2. Experimental Section

2.1. Synthesis of Cobalt Nanoparticles Using a Polymeric Microfluidic Reactor. Cobalt nanoparticles were prepared in the

(5) (a) Cha, I. S.; Mo, B. C.; Kim, T. K.; Hong, H. S. *J. Mater. Res.* **2005**, *20* (8), 2148. (b) Tanori, J.; Pileni, M. P. *Langmuir* **1997**, *13* (4), 639. (c) Lisiecki, I.; Pileni, M. P. *J. Am. Chem. Soc.* **1993**, *115*, 3887. (d) Murray, C. B.; Sun, S.; Gaschler, W.; Doyle, H.; Betley, T. A.; Kagan, C. R. *IBM J. Res. Dev.* **2001**, *45* (1), 47. (e) Sun, S.; Murray, C. B. *J. Appl. Phys.* **1999**, *85* (8, Part 2A), 4325. (f) Peng, X.; Wickham, J.; Alivisatos, A. P. *J. Am. Chem. Soc.* **1998**, *120* (21), 5343.

(6) (a) Puntes, V. F.; Zanchet, D.; Erdonmez, C. K.; Alivisatos, A. P. *J. Am. Chem. Soc.* **2002**, *124* (43), 12874. (b) Dumestre, F.; Chaudret, B.; Amiens, C.; Respaud, M.; Fejes, P.; Renaud, P.; Zurcher, P. *Angew. Chem., Int. Ed.* **2003**, *42* (42), 5213. (c) Dumestre, F.; Amiens, C.; Chaudret, B.; Fromen, M. C.; Casanove, M. J.; Renaud, P.; Zurcher, P. *Mater. Res. Soc. Symp. Proc.* **2003**, *735*, 165 (Bioinspired Nanoscale Hybrid Systems). (d) Dumestre, F.; Chaudret, B.; Amiens, C.; Fromen, M.-C.; Casanove, M.-J.; Renaud, P.; Zurcher, P. *Angew. Chem., Int. Ed.* **2002**, *41* (22), 4286. (e) Wang, Z. L. *J. Phys. Chem. B* **2000**, *104* (6), 1153. (f) Wang , Z. L.; Dai, Z.; Sun, S. *Adv. Mater.* **2000**, *12*, 1944.

(7) Fletcher, D. I.; Haswell, S. J.; Pombo-Villar, E.; Warrington, B. H.; Watts, P.; Wong, Y. F. S.; Zhang, X. *Tetrahedron* **2002**, *58*, 4735.

(8) Chan, M. E.; Mathies, R. A.; Alivisatos, A. P. *Nano Lett.* **2003**, *3* (2), 199.

(9) Song, Y.; Kumar, C. S. S. R.; Hormes, J. *J. Micromech. Microeng.* **2004**, *14* (7), 932.

(10) (a) Song, Y.; Kumar, C. S. S. R.; Hormes, J. *J. Nanosci. Nanotechnol.* **2004**, *4* (7), 788. (b) Song, Y.; Doomes, E. E.; Prindle, J.; Hormes, J.; Kumar, C. S. S. R. *J. Phys. Chem. B* **2005**, *109* (19), 9330.

(11) Hyeon, T. *Chem. Commun.* **2003**, 927.

(12) Sun, S.; Murray, C. B. *J. Appl. Phys.* **1999**, *85* (8), 4325.

(13) Min, B. I.; Oguchi, T.; Freeman, A. *J. Phys. Rev. B* **1986**, *33* (11), 7852.

(14) Ram, S. *Acta Mater.* **2001**, *49*, 2297.

(15) Nie, X.; Jiang, J. C.; Meletis, E. I.; Tung, L. D.; Spinu, L. *J. Appl. Phys.* **2003**, *93* (8), 4750.

(16) Calvo, F.; Doye, J. P. K. *Phys. Rev. B: Condens. Matter* **2004**, *69* (12), 125414/1.

(17) Huang, J. Y.; Wu, Y. K.; Ye, H. Q. *Appl. Phys. Lett.* **1995**, *66* (3), 308.

(18) Wilcoxon, J. P.; Provencio, P. P. *J. Phys. Chem. B* **1999**, *103* (45), 9809.

(19) Lin, X. M.; Sorensen, C. M.; Klabunde, K. J.; Hajipanayis, G. C. *J. Mater. Res.* **1999**, *14* (4), 1542.

(20) Qadri, S. B.; Skelton, E. F.; Dinsmore, A. D.; Hu, J. Z.; Kim, W. J.; Nelson, C.; Ratna, B. R. *J. Appl. Phys.* **2001**, *89* (1), 115.

(21) Margeat, O.; Amiens, C.; Chaudret, B.; Lecante, P.; Benfield, R. E. *Chem. Mater.* **2005**, *17* (1), 107.

(22) (a) Leuschner, C.; Kumar, C. S. S. R.; Hormes, J.; Hansel, W. *J. Biomed. Nanotechnol.* **2005**, *1* (2), 229. (b) Modrow, H.; Palina, N.; Kumar, C. S. S. R.; Doomes, E. E.; Aghasyan, M.; Palshin, V.; Tittsworth, R.; Jiang, J. C.; Hormes, J. *Phys. Scr.* **2005**, *T115*, 790. (c) Zonghuan, L.; Malcolm, D. P.; Guo, Z.; Vladimir, O. G.; Kumar, C. S. S. R.; Yuri, M. L. *Langmuir* **2005**, *21* (5), 2042. (d) Guo, Z.; Kumar, C. S. S. R.; Henry, L. L.; Doomes, E. E.; Hormes, J.; Podlaha, E. J. *J. Electrochem. Soc.* **2005**, *152* (1), D1. (e) Hormes, J.; Modrow, H.; Bonnemann, H.; Kumar, C. S. S. R. *J. Appl. Phys.* **2005**, *97* (10, Part 3), 10R102/1. (f) Bala, G. N.; Michelle, C. U.; Hormes, J.; Kumar, C. S. S. R.; Todd, M. W. *Biotechnol. Prog.* **2006**, *22*, 91. (g) Kumar, C. S. S. R.; Leuschner, C.; Doomes, E. E.; Henry, L. L.; Juban, M.; Hormes, J. J. *Nanosci. Nanotechnol.* **2004**, *4* (3), 245. (h) Kumar, C. S. S. R.; Aghasyan, M.; Modrow, H.; Hormes, J.; Tittsworth, R. *J. Metastable Nanocryst. Mater.* **2004**, *23*, 343.

(23) Held, G. A.; Grinstein, G.; Doyle, H.; Sun, S.; Murray, C. B. *Phys. Rev. B* **2001**, *64*, 2408.

(24) Dinega, D. P.; Bawendi, M. G. *Angew. Chem., Int. Ed.* **1999**, *38*, 1788.

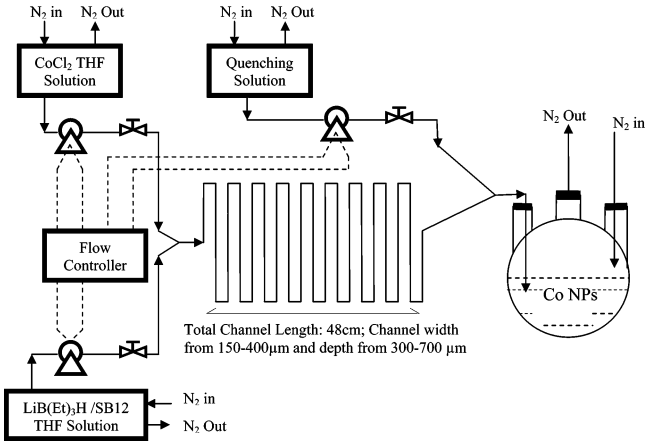

Figure 1. Schematic of the microfluidic reactor process for phase-controlled synthesis of cobalt nanoparticles.

microreactor by the reduction of $CoCl_2$ in tetrahydrofuran (THF) using lithium hydrotriethylborate ($LiBH(C_2H_5)_3$) as a reducing agent and 3-(*N*,*N*-dimethyldodecylammonia)propanesulfonate (SB12) as a stabilizer according to the chemical reaction given as follows.[9,10a,26,27]

$$C_{12}H_{25}N(CH_3)_2(C_3H_6{-}SO_3) + LiBEt_3H \xrightarrow{THF} C_{12}H_{25}N(CH_3)_2(C_3H_6{-}SO_3)\cdot LiBEt_3H$$

$$C_{12}H_{25}N(CH_3)_2(C_3H_6{-}SO_3) + LiBEt_3H + CoCl_2 \xrightarrow{THF} Co_{colloid}\cdot C_{12}H_{25}N(CH_3)_2(C_3H_6{-}SO_3)\cdot LiCl + BEt_3 + {}^1/_2H_2$$

THF (99.90% pure packaged under nitrogen), $CoCl_2$ (99.9%, anhydrous), lithium hydrotriethyl borate as a 1 M solution in THF, SB12, acetone (reagent anhydrous, water < 0.5%, 99.9+%), and ethanol (reagent anhydrous, water < 0.003%) were purchased from Aldrich Chemical Co. and used without further purification.

Figure 1 shows the schematic of the microfluidic reactor process. The saturated $CoCl_2$/THF solution (4 g/L) and the reducing agent solution (complex of $Li[B(Et)_3H]$ with SB12 in THF, with SB12 of 3.4 g/L and 200 mL of 1 mM $Li[B(Et)_3H$ THF solution) are delivered into the microfluidic reactor using self-priming pumps (120SPI-30, Bio-Chem Valve, Inc.). The produced nanoparticles are collected in the receiver flask and may be quenched by a mixture of ethanol and THF (1:3, v/v) just before entering into the receiver. Three experiments were performed with different flow rates while quenching the reaction differently. The first experiment was conducted at a flow rate of 0.9 mL/min. The formed nanocolloid solution was quenched immediately at the outlet of the microfluidic reactor. The second experiment was performed at a flow rate of 0.08 mL/min, and the formed nanocolloid solution was again quenched immediately at the outlet of the microfluidic reactor. The third experiment was performed at a flow rate of 0.08 mL/min, and the formed nanocolloid solution was left undisturbed for more than 8 h and then quenched by adding a mixture of ethanol and THF (1:3, v/v) dropwise. All these experiments were performed under inert gas protection. After the precipitation of Co nanoparticles, the supernatant solution was decanted and the particles were washed three times using a mixture of ethanol and THF (25 vol % ethanol) and then dried to obtain a fine black powder.

2.2. In Situ XANES Analysis of the Liquid Co Nanocolloids. A schematic drawing of the experimental setup for obtaining in situ XANES data is shown in Figure 2. The outlet of the microfluidic reactor is connected to a sealed liquid cell that has a Kapton film window. Co nanocolloid is collected into the liquid cell just before entering the product flask. The cell is closed once it is filled with the sample solution, and the XANES data are obtained. The procedure adopted is very similar to the one reported in the literature for in situ characterization of copper nanocolloid formation.[10b]

2.3. Characterization of Cobalt Nanoparticles. The particle size, shape, and distribution were characterized using the transmission electron microscopy (TEM; transmission electron microscope 2010, 200 KV, JEOL). Samples for TEM analysis were prepared by placing a drop of well-suspended Co nanoparticles in oxygen-free water or ethanol on a carbon-coated copper TEM grid at room temperature and allowing the solvent to evaporate. The nanoparticle crystal structures were characterized by SAED, XRD, and XANES. SAED was operated in the JEOL 2010 transmission electron microscope at the wavelength of 0.0252 Å. Powder XRD measurement was carried out for the powder Co samples with monochromatized Co Kα radiation ($\lambda = 1.7890$ Å) using the INEL CPS120 curved position sensitive detector system. The samples are placed in a special holder to prevent exposure to air. XANES experiments were performed at the X-ray microprobe double crystal monochromator beamline at port 5A of the Center for Advanced Microstructures and Devices (CAMD) synchrotron radiation source at Louisiana State University.[28] The storage ring was operated at an electron beam energy of 1.3 GeV. For these Co K-edge XANES measurements, the beamline monochromator was calibrated with a 7.5 μm hcp cobalt foil. Ge(220) crystals provided monochromatic X-rays in the region of interest. The energy bandwidth for the excitation radiation was less than 2 eV over the range of energies examined. Spectra were background subtracted and normalized using standard procedures.[29,30]

Magnetic data were obtained using a Quantum Design MPMS-5S SQUID magnetometer system.[10c−e] The measurements were carried out on samples consisting of the dried powder packed into a gelatin capsule with cotton placed inside the capsule to keep the powder stationary. The samples were prepared under inert gas conditions in a drybox, and care was taken to minimize air exposure to the gel cap containing the sample as the gel cap was transferred to the magnetometer for measurements. Both magnetization, *M*, versus temperature, *T*, and magnetization versus applied magnetic field, *H*, measurements were performed. Before inserting a sample

(25) (a) Edel, E. B.; Fortt, R.; deMello, J. C.; deMello, A. *J. Chem. Commun.* **2002**, 1136. (b) Chan, M. E.; Mathies, R. A.; Alivisatos, A. P. *Nano Lett.* **2003**, *3*, 199. (c) Kawa, M.; Morii, H.; Ioku, A.; Saita, S.; Okuyama, K.; *J. Nanopart. Res.* **2003**, *5*, 81. (d) Ayon, A. A.; Braff, R. A.; Bayt, R.; Sawin, H. H.; Schmidt, M. A. *J. Electrochem. Soc.* **1999**, *146*, 2730. (e) Jongen, N.; Donnet, M.; Bowen, P.; Lemaitre, J.; Hofmann, H.; Schenk, R.; Hofmann, C.; Aoun-Habbache, M.; Guillemet-Fritsch, S.; Sarrias, S.; Rousset, A.; Viviani, M.; Buscaglia, M. T.; Buscaglia, V.; Nanni, P.; Testino, A.; Herguijuela, J. R. *Chem. Eng. Technol.* **2003**, *26*, 303. (f) Buscaglia, M. T.; Buscaglia, V.; Viviani, M.; Testino, A.; Nanni, P.; Bowen, P.; Donnet, M.; Natalie, J.; Rainer, S.; Hofmann, C.; Hessel, V.; Schonfeld, F. *Adv. Sci. Technol.* **2003**, *30*, 535 (Faenza, Italy, 10th International Ceramics Congress, 2002, Part A). (g) Wei, G.; Huang, H. Y.; Xiong, R. C. *Chin. Chem. Lett.* **2003**, *14* (8), 877. (h) He, S.; Kohira, T.; Uehara, M.; Kitamura, T.; Nakamura, H.; Miyazaki, M.; Maeda, H. *Chem. Lett.* **2005**, *34* (6), 748. (i) Kim, K. D.; Kim, H. T. *Mater. Lett.* **2003**, *57* (21), 3211.
(26) Bonnemann, H.; Braun, G.; Brijoux, W.; Brinkmann, R.; Schulze, A. T.; Seevogel, K.; Siepen, K. *J. Organomet. Chem.* **1996**, *520*, 143.
(27) Glavee, G. N.; Klabunde, K. J.; Sorensen, C. M.; Hadjipanayis, G. C. *Inorg. Chem.* **1993**, *32* (4), 474.
(28) (a) Craft, B. C.; Feldman, M.; Morikawa, E.; Poliakoff, E. D.; Saile, V.; Scott, J. D.; Stockbauer, R. L. *Rev. Sci. Instrum.* **1992**, *63*, 1561. (b) Morikawa, E.; Scott, J. D.; Goettert, J.; Aigeldinger, G.; Kumar, C. S. S. R.; Craft, B. C.; Sprunger, P. T.; Tittsworth, R. C.; Hormes, J. *Rev. Sci. Instrum.* **2002**, *73*, 3.
(29) Koningsberger, D. C.; Prins, R. *X-ray Absorption - Principles, Applications, Techniques of EXAFS, SEXAFS and XANES*; Wiley and Sons: New York, 1988; Vol. 92.
(30) Teo, B. K. *EXAFS: Basic principles and data analysis;* Springer-Verlag: New York, 1986.

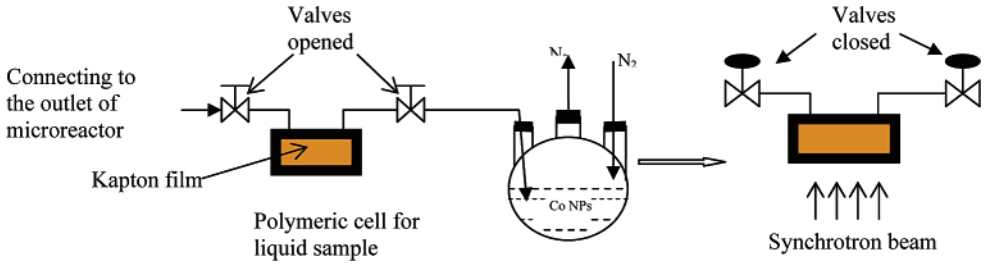

Figure 2. Schematic diagram for in situ Co-XANES experiments.

in the sample space of the magnetometer, a short program sequence was performed which cycles the magnetic field from +5 T to 0 by alternating between decreasing positive and negative values to minimize any remnant magnetic field at the location where the sample was placed. Hence, when the applied magnetic field is set to 0 G the remnant magnetic field at the sample location will be negligible. This should minimize any offset when the applied magnetic field is set to 0 G. Furthermore, to reduce the possibility of the sample contamination by air that may leak into the sample chamber the temperature is periodically raised to 300 K and the sample chamber purged. The measurement sequence is set up in such a way that the *M* versus *H* set of measurements is performed after the *M* versus *T* set of measurements are completed.

For the *M* versus *T* data, both zero field cooled (ZFC) and field cooled (FC) measurements were made. For the ZFC measurements the sample was first cooled from room temperature to 10 K in zero applied magnetic field. The applied magnetic field was then set to 100 G, and the ZFC data were collected as the sample temperature was increased to the maximum. The FC data were collected as the temperature was cycled back to 10 K.

3. Results and Discussion

In addition to the ability to vary temperature and concentration reproducibly on a microscale, the main advantage of microfluidic reactors for nanoparticle synthesis, as demonstrated in this paper, is that the reaction can be quenched continuously at the outlet through destruction of excess reducing agent using acetone or another relevant solvent in the product flask. This provides an opportunity to prevent further nucleation and growth of particles once they leave the microreactor and offers an opportunity to distinctly separate nanocrystal nucleation and growth.[31] The effect of flow rate within a microreactor on size and size distribution of nanoparticles was recently demonstrated by several research groups.[25,31a] The unique features of the microreactor can be used to fine-tune not only the size but also the anisotropic shapes.[32] To investigate the effect of flow rates on cobalt nanoparticles obtained, we have selected two different flow rates. When the reaction was carried out at a flow rate of 0.9 mL/min and quenched immediately, spherical cobalt nanoparticles with an average size of 3.9 ± 0.9 nm were obtained (Figure 3a−c, the first experiment). The five diffraction rings in the SAED pattern (Figure 3b) correspond to lattice spacings of 2.14, 1.83, 1.31, 1.12, and 0.85 Å, which agrees well with those of the (111), (200), (220), (311), and (331) reflections of the (fcc) β Co, respectively. However, the presence of minor impurities from the hcp phase is also noticed from the presence of weak rings which can be assigned to the (102) plane, (201) plane, and (004) plane in hcp Co, respectively. The lattice constant of Co nanoparticles calculated for the fcc phase is about 3.69 Å, slightly larger than that of the bulk fcc Co.[15,33] When the flow rate was reduced to 0.08 mL/min and the product was quenched immediately, spherical cobalt nanoparticles were obtained with an average size of 3.5 ± 0.7 nm (Figure 3d−f, the second experiment), which corresponds within the error margins to the particle size of the fcc particles. However, the five diffraction rings in the SAED pattern (Figure 3e) have lattice spacings of 2.17, 2.01, 1.90, 1.30, and 1.08 Å that can be indexed as the (100), (002), (101), 102, (110), (200), (103), and (112) reflections of hcp Co, respectively, with lattice constants of $a = 2.58$ Å and $c = 4.18$ Å, slightly larger than that of bulk hcp Co.[34,35] Additionally, when the product obtained under this flow rate was left undisturbed for a longer period without quenching (>8 h, the third experiment), the TEM image showed formation of larger spherical particles with an average size of 4.7 ± 1.3 nm (Figure 3g,i), again in accordance with the sizes obtained for fcc and hcp particles. But now, the six diffraction rings in the SAED pattern (Figure 3h) are indexed as lattice spacings of 2.681, 2.168, 2.051, 1.971, 1.851, 1.615, 1.425, 1.343, 1.205, and 1.140, which agree well with those of the (210), (220), (221), (310), (311), (321), (330), (420), (510), and (520) reflections, respectively, of ϵ cobalt as reported in the literature.[11−12,15,24,33]

To make sure that all the reflection rings are not affected by possible trace impurities from either oxides or borides of cobalt, elemental analysis (energy dispersive analysis of X-rays) was done for all three samples, shown in Figure 4. There was no trace of boron found in these samples, indicating that the boron byproducts were removed completely by the washing process. The analysis for these three samples suggested that the fcc Co nanoparticles were almost pure Co (Figure 4a). The oxygen content for the hcp Co nanoparticles (Figure 4b) and the ϵ Co nanoparticles (Figure 4c) were far from the lowest oxidization state of Co (or CoO), which was probably introduced from residual surfactant or the handling process during sample preparation to give the Co nanoparticles a very thin oxidized layer. These results are consistent with the SAED analysis.

(31) (a) DeMello, J.; DeMello, A. *Lab Chip* **2004**, *4*, 11N. (b) Murray, C. B.; Kagan, C. R.; Bawendi, M. G. *Annu. Rev. Mater. Sci.* **2000**, *30*, 545.
(32) Manna, L.; Scher, C. E.; Alivisatos, P. A. *J. Am. Chem. Soc.* **2000**, *122* (51), 12700.
(33) Cullity, B. D.; Stock, S. R. *Elements of X-Ray Diffraction*, 3rd version; Prentice Hall: Upper Saddle River, NJ, 2001; Appendix 5.
(34) Dimitrov, D. V.; Hadjipanayis, G. C.; Papaefthymiou, V.; Simopoulos, A. *IEEE Trans. Magn.* **1997**, *33* (5), 4363.
(35) Zhang, P.; Sham, T. K. *Phys. Rev. Lett.* **2003**, *90*, 245502.

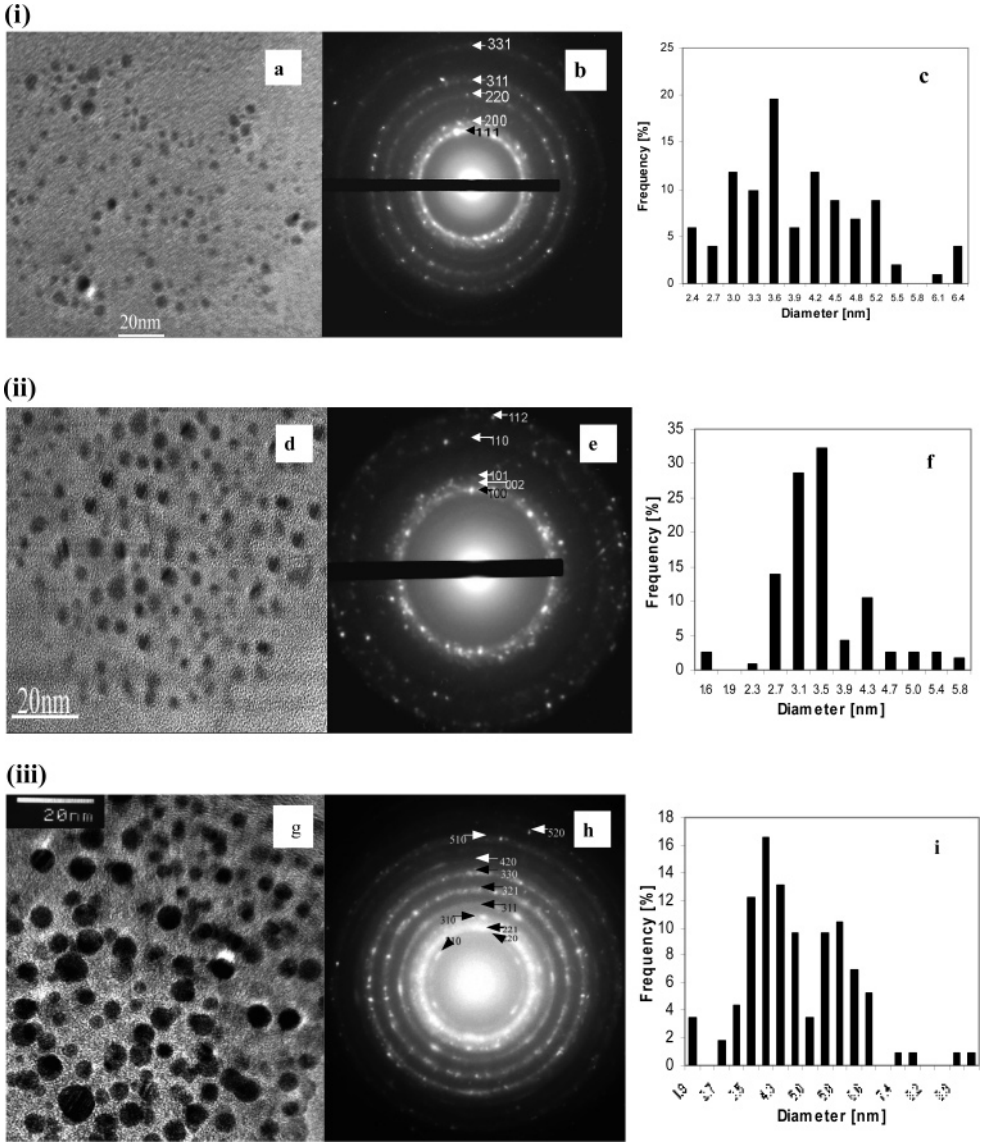

Figure 3. TEM image, SAED patterns, and histograms: (i) a−c, fcc Co nanoparticles obtained at high flow rate and quenched at the outlet of the microfluidic reactor. (ii) d−f, hcp Co nanoparticles obtained at low flow rate and quenched at the outlet of the microfluidic reactor. (iii) g−i, ϵ Co nanoparticles obtained at low flow rate with delayed quenching.

The crystal structures of three Co nanoparticles were also determined by the XRD spectrum (Figure 5). Not surprisingly, as the particle size is less than 5 nm, one broad peak which can be a composite of crystalline lines was obtained from 45 to 60° (2θ). This region falls at the major peak positions corresponding to (111) of fcc Co, (100), (002), and (101) of hcp Co, and (221), (310), and (311) of ϵ Co were obtained.[12,19,36] Again these patterns showed no peaks related to cobalt oxides because the samples were handled under inert protection.

XANES spectroscopy, which is highly sensitive to structural changes of small nanoparticles as a result of its nature as a local probe technique,[35,37−39] was used as a third method to confirm the crystal structures of the as-prepared Co nanoparticles (Figure 6). To identify the characteristic features of the three Co phases, real space Full Multiple Scattering (FMS) calculations were performed using the FEFF8 code,[40] whose output has been shown to provide meaningful results for a broad range of systems. Evidently, the most significant changes are observed in the region of the absorption edge. However in experimental data, which do feature broadening, the only significant change in structure A which can be expected to be resolvable is the slightly delayed onset and slightly reduced intensity in the case of

(36) Cullity, B. D. *Introduction to magnetic materials*; Addison-Wesley Publishing cocmpany, Inc.: Menlo Park, CA, 1972; Chapter 1, pp 7 and 17, and Chapter 7, p 357.
(37) Chen, L. X.; Liu, T.; Thurnauer, M. C.; Csentcits, R.; Rajh, T. *J. Phys. Chem. B* **2002**, *106*, 8539.
(38) Modrow, H.; Bucher, S.; Hormes, J.; Brinkmann, R.; Bönnemann, H.; *J. Phys. Chem. B* **2003**, *107*, 3684.
(39) Kumar, C. S. S. R.; Aghasyan, M.; Modrow, H.; Doomes, E. E.; Henke, C.; Hormes, J.; Tittsworth, R. *J. Nanopart. Res.* **2004**, *6*, 369.
(40) (a) Ankudinov, A. L.; Ravel, B.; Rehr, J. J.; Conradson, S. D. *Phys. Rev. B* **1998**, *58*, 7565. (b) Modrow, H.; Bucher, S.; Rehr, J. J.; Ankudinov, A. *Phys. Rev. B* **2003**, *67*, 035123. (c) Gilbert, B.; Frazer, B. H.; Belz, A.; Conrad, P. G.; Nealson, K. H.; Haskel, D.; Lang, J. C.; de Stasi, G. *J. Phys. Chem. A* **2003**, *107*, 2839. (d) Hallmeier, K. H.; Uhlig, L.; Szargan, R. J. *J. Electron Spectrosc. Relat. Phenom.* **2002**, *122*, 91. (e) Reich, A.; Panthöfer, M.; Modrow, H.; Wedig, U.; Jansen, M. *J. Am. Chem. Soc.* **2004**, *126*, 14428.

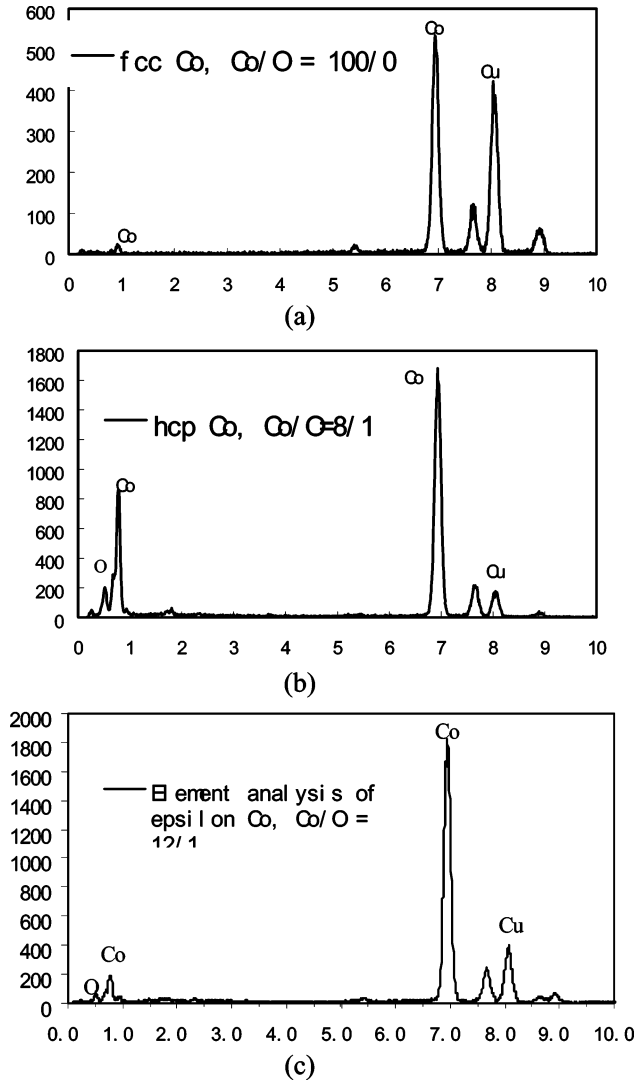

Figure 4. Elemental analysis of Co nanoparticles of three different phases: (a) fcc, (b) hcp, and (c) ϵ.

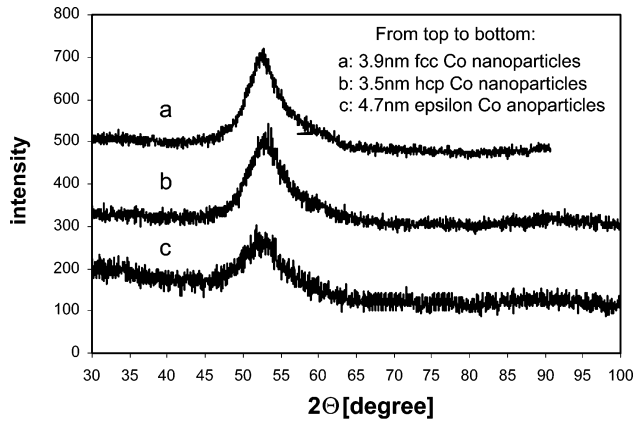

Figure 5. XRD spectra for 2θ (degree) Co nanoparticles with different crystal structures.

the ϵ Co phase (Figure 6g). More resolving power resides in the intensity and energy splitting between resonances B and C: with respect to the intensity, B is stronger in fcc Co (Figure 6f), whereas C is dominant in the hcp (Figure 6h) and ϵ phases. With respect to the splitting, it is reduced from fcc via hcp to the ϵ phase, where the maximum of structure C is located at a different energy position.

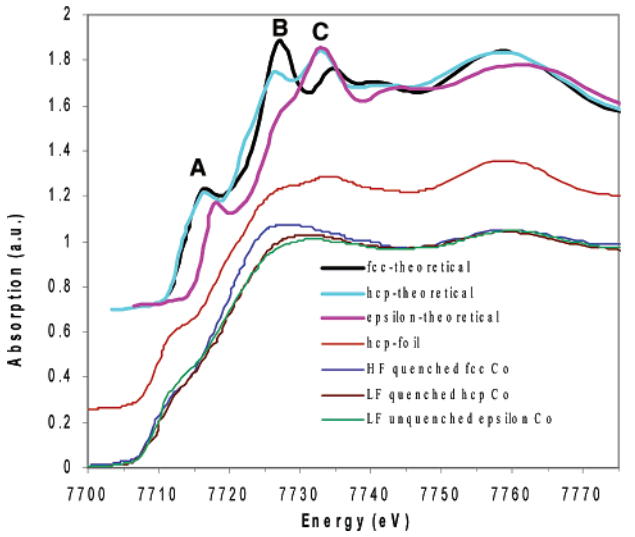

Figure 6. Ex situ Co K XANES spectra: a (dark blue), fcc Co nanoparticles synthesized at high flow rate and quenched immediately; b (green), hcp Co nanoparticles synthesized at low flow rate and quenched immediately; c (brown), Co nanoparticles synthesized at low flow rate with delayed quenching; d (red), hcp Co foil; e (light blue), theoretical hcp Co; f (black), theoretical fcc Co; and g (pink), theoretical ϵ Co.

Looking at the spectra of the as-synthesized particles, it turns out that they are free from oxidative impurities because neither significant chemical shift of the absorption edge to higher energy, lower pre-edge intensity, nor a systematically higher white line intensity are observed. Also, the presence of the shape resonance at about 7760 eV indicates that one is dealing with a Co metal phase. In comparison to the theoretical calculations and the reference foil (Figure 6d), the spectral features are broadened, and their intensity is damped and no longer allows for the full resolution of features B and C, respectively. This is expected, as surface relaxation effects increase the width of the radial distribution function and surface atoms have a reduced number of backscattering atoms in their neighborhood. Still, the general features of the respective phases can be assigned to the spectra of the observed material: The maximum of the spectrum in Figure 6a coincides with the position expected for fcc Co, the spectrum in Figure 6b corresponds well to the shape of hcp Co, and the spectrum in Figure 6c shows the slightly delayed onset of absorption and shifted maximum position typical for the ϵ Co phase. Thus, the SAED analysis is confirmed by the XANES spectra.

In principle, two explanations for the appearance of three different phases come to mind: On one hand, the product obtained at the outlet of the reactor is more advanced on the time scale in the case of slow flow rate; thus, one may imagine that after formation of fcc particles, these convert to hcp in a quick reaction step. On the other hand, one might obtain different products as a function of the flow conditions having a common hcp-like intermediate as described in Figure 10. To gain some understanding of at what stage in the microreactor the different phases are formed, in situ XANES spectroscopy was carried out on liquid samples coming out of the outlet of the microreactor using the setup shown in Figure 2. Figure 7 shows the XANES spectrum of Co nanoparticle solutions at low flow rates (<0.08 mL/min) after growing for zero min, 3 h, and more than 8 h. The

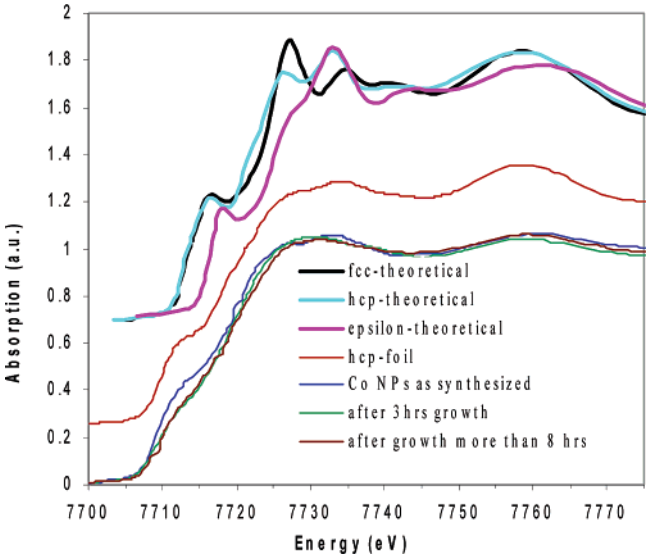

Figure 7. In situ Co K-edge XANES spectra of Co nanoparticles formed at low flow rate and their ripening process: a (black), theoretical fcc (β) Co; b (pink), theoretical ϵ Co; c (light blue), theoretical hcp (α) Co; d (red), hcp Co foil; e (dark blue), Co nanoparticles as synthesized; f (green), Co nanocolloid solution obtained after 3 h of growth; and g (brown), Co nanoparticles obtained after growing more than 8 h. Note the phase transition which appears to be visible after 3 h of ripening time.

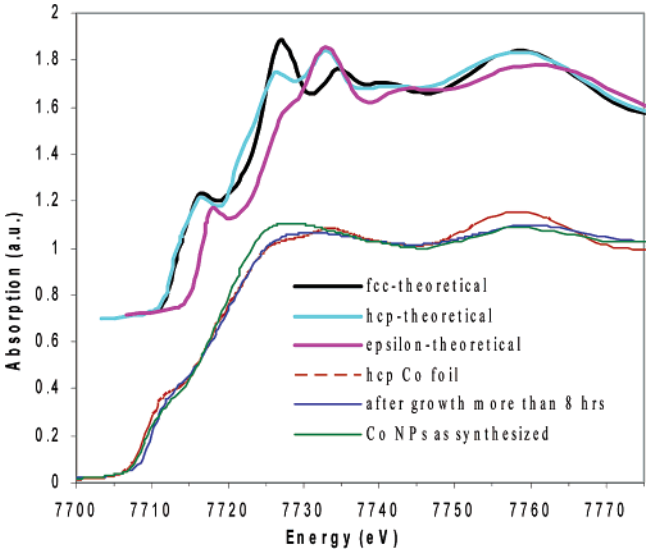

Figure 8. In situ Co K-edge XANES spectrum of Co nanoparticles formed at high flow rate: a (black), theoretical fcc (β) Co; b (pink), theoretical ϵ Co; c (light blue), theoretical hcp (α) Co; d (green), fresh Co nanocolloid solution; e (dark blue), Co nanoparticles obtained after long time growth; and f (red), hcp Co foil.

reference spectra of the Co nanoparticles obtained after the workup are also provided. Using the same arguments for determination of the respective phases of Co as detailed above, one can reconfirm directly the previous phase assignment: The in situ XANES spectrum taken immediately after the particles leave the microreactor reconfirms the ex situ result that the hcp (α) phase (Figure 7e) is formed at low flow rate. With increasing time, this phase is transformed to ϵ phases (Figure 7f,g) after the Co colloid solutions are undisturbed for 3 h or more.

Figure 8 shows the in situ XANES spectrum of Co nanoparticles coming out of the microreactor at high flow rate (0.9 mL/min). Again, the in situ XANES spectrum taken directly after passage through the reactor confirms the results of the ex situ measurement, that is, that the Co nanoparticles are mainly formed in the fcc (β) phase using the same arguments as for the ex situ case (Figure 8d,e). As the measurement takes about 15 min, the "age" of the sample is comparable to the age of the one obtained using low flow rate; still no conversion to hcp is observed. However, if the material is aged under these conditions, after several hours again conversion to the ϵ phase is observed. Therefore, one can conclude that hcp is merely an intermediate product between the fcc and the ϵ phase. In fact, bearing in mind the similarity of the particle size between fcc and hcp, such an intermediate state would not be difficult to explain.

The data from the in situ XANES analysis demonstrate that either fcc or hcp structure formation takes place within the microfluidic channels governed by the flow rate. As discussed below in detail, this observation suggests that the flow rate influences the nucleation process. Even though one could control the crystal structure of the Co nanoparticles obtained, it is obvious from the TEM images that the Co nanoparticles obtained are far from monodisperse and requires an additional purification step to narrow the size distribution. However, because of the convenient possibility to synthesize large quantities of material by our approach, application of an additional size-selection step[1,2,41] to improve the monodispersity of the obtained particles should be unproblematic.

Magnetic properties for Co nanoparticles with different structures were measured as described in the experimental section. The results are displayed in Figure 9. The blocking temperatures (T_b) for each phase can be determined from the maximum in ZFC magnetization versus temperature data. T_b is the temperature below which the magnetization of the particles can spontaneously align; that is, the material becomes ferromagnetic. The data for each of the samples show characteristic behavior with the ZFC magnetization increasing as the temperature is increased. In the case of the fcc Co and hcp Co samples, the magnetization decreases as the temperature is increased above T_b. As the temperature is now decreased the FC magnetization increases and becomes nearly flat as the temperature approaches the lowest values (Figure 9A). For the fcc Co and the hcp Co nanoparticles the ZFC goes through a maximum indicating the blocking temperature is reached (fcc Co, $T_b = 130$ K, and hcp Co, $T_b = 274$ K). However, the ϵ Co ZFC data show no maximum over the measurement range indicating a T_b greater than 330 K.

When T_b and the particle diameters given earlier are used, it is possible to obtain estimates of the anisotropy constants for the different phases. The anisotropy constant K is related to the energy barrier that must be overcome for the realignment of the magnetic moments as the particle acquires stability in the ferromagnetic state. K is related to T_b by the relation $K = 25k_BT_b/V$ where k_B and V are the Boltzmann constant and the volume of the particle, respectively. TEM

(41) (a) Jang, J.; Yoon, H. *Small* **2005**, *1* (12), 1195. (b) Anand, M.; McLeod, M. C.; Bell, P. W.; Roberts, C. B. *J. Phys. Chem. B* **2005**, *109* (48), 22852. (b) Cushing, B. L.; Kolesnichenko, V. L.; O'Connor, C. J. *Chem. Rev.* **2004**, *104*, 3893.

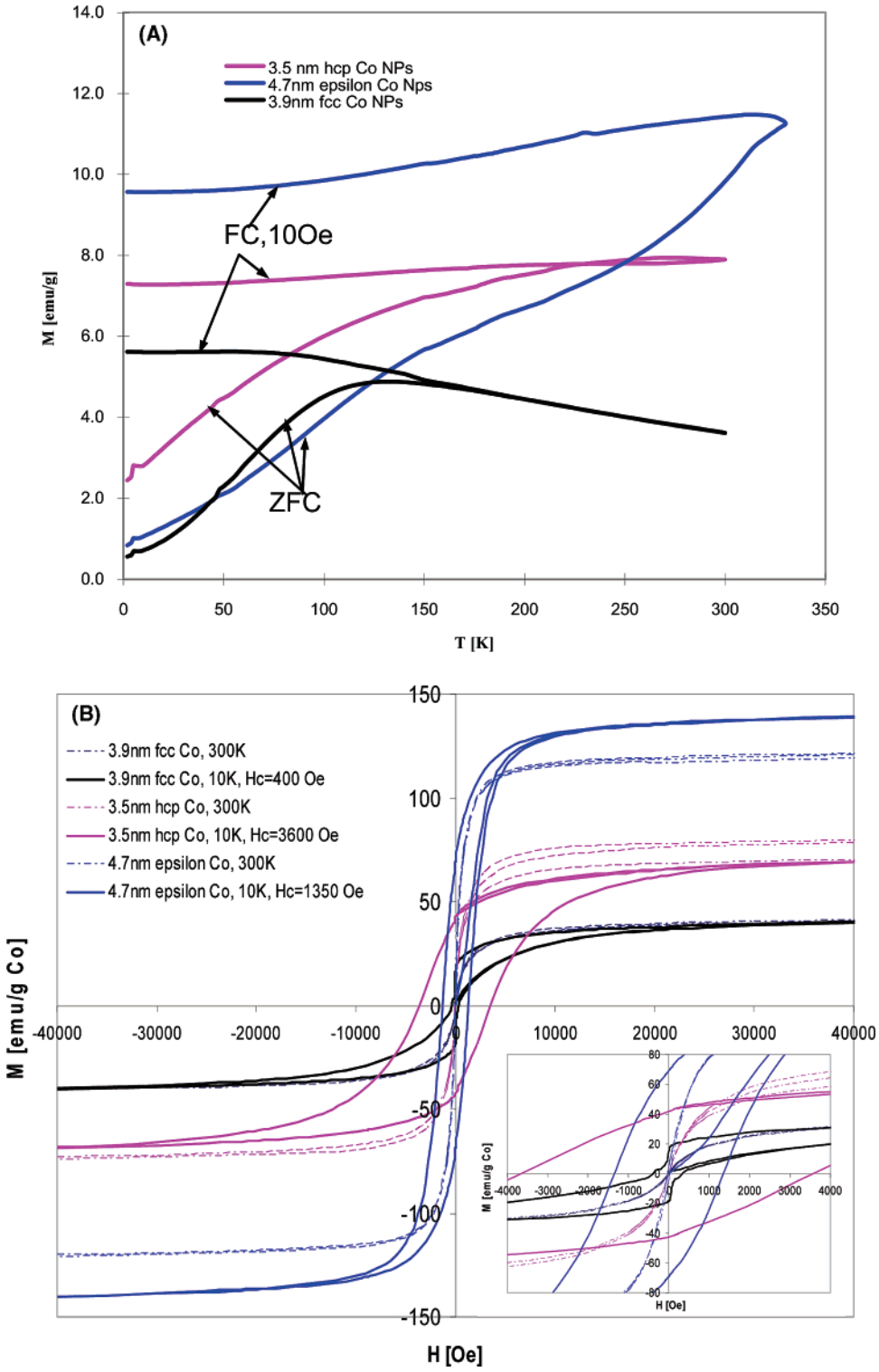

Figure 9. (A) ZFC/FC magnetization for Co nanoparticles with different crystal structures. (B) Hysteresis loops for Co nanoparticles with different crystal structures.

analysis indicates that the particles are spherical in shape, so the volume can be easily calculated. Table 1 gives the calculated values for *K*. Our fcc Co value is significantly higher than that of bulk fcc Co (2.7×10^6 emu/g) as reported by Petit et al. and also the values reported from their work (2.4×10^6 emu/g).[42] In the same paper it is also pointed out that the anisotropy of the nanoparticle form is usually higher than that of the bulk and that aggregation tends to drive the anisotropy constant toward the bulk value. The high value that we obtained for our samples would then suggest that aggregation is negligible and the nanoparticles in our samples are well-separated from each other. This is supported by the TEM results which show that the particles are not aggregated. The anisotropy constants for the other phases, hcp Co and ϵ Co, are 4.2×10^7 erg/cm^3 and in excess of 2.1×10^7 erg/cm^3, respectively.

(42) Petit, C.; Taleb, A.; Pileni, M. P. *J. Phys. Chem. B* **1999**, *103*, 1805.

Table 1

sample structure	particle size (nm)	$K \times 10^7$ (erg/cm^3)	M_s (emu/g)	M_r (emu/g)	M_r/M_s	H_c (G)	μ_B/atom	T (K)
fcc Co	3.9	1.4	41	1	0.03	30	0.43	300
hcp Co	3.5	4.2	81	1.0	0.01	10	0.86	300
ϵ Co	4.7	>2.1	124	5	0.04	37	1.31	300
fcc Co	3.9	1.4	39	15	0.38	390	0.41	10
hcp Co	3.5	4.2	66	38	0.54	3900	0.70	10
ϵ Co	4.7	>2.1	142	73	0.51	1400	1.5	10

To examine the magnetic field dependence of the magnetization (M vs H), the magnetization was measured as the applied magnetic field was cycled from 0 to +5 T to −5 T and back to +5 T. M versus H data was collected at 300 and 10 K (Figure 9B). All the data show hysteresis with hcp Co showing the largest and ϵ Co exhibiting the least. The fcc Co magnetization at $T = 300$ and 10 K shows significant overlap in the hysteresis curves, and the saturation magnetization data at $T = 300$ K exceeds the data at 10 K. At $T = 300$ K the saturation magnetization, M_s, is 81 (emu/g) and 124 (emu/g) for hcp Co and ϵ Co, respectively, and at $T = 10$ K the respective values of M_s are 66 (emu/g) and 142 (emu/g). The low temperature (10 K) saturation magnetization M_s values for all the samples are significantly lower than for bulk Co (163 emu/g): fcc Co, $M_s = 39$ emu/g; hcp Co, $M_s = 66$ emu/g; and ϵ Co, $M_s = 142$ emu/g. The low value for the fcc phase compared with that for the bulk is consistent with the finding by Petit et al. who report a value of 80 emu/g for Co nanoparticles dispersed in pyridine.[42]

It is well-established that, depending on the chemical nature of the surface adsorbate on magnetic nanoparticles, the magnetic properties will vary.[43] This is believed to be the cause of the decreased saturation magnetization that the present samples exhibit. The values of M_s at $T = 300$ K are shown for comparison.

The room-temperature saturation magnetization for bulk Co is ~163 emu/g. The magnetic moment/atom μ_H was calculated using the saturation magnetization values. The results are given in Table 1. The calculated values for μ_H are reduced compared with that of the bulk Co ($\mu_H = 1.70$ and 1.72 at 300 and 0 K, respectively). The reduced magnetic moment is attributed to both a size effect and remnants of the surfactant used in the sample preparation. The squareness factor M_r/M_s for the hysteresis curves at 300 K shows strong deviation from unity at 300 K with the ϵ Co phase having the largest value of 0.04, and the fcc Co phase has a value of 0.03. However, at 10 K the values are significantly closer to 1. The squareness factor has implications for technological applications.

At 10 K, the 3.5 nm hcp Co nanoparticles show a larger coercivity of 3900 Oe than the 3.9 nm fcc Co nanoparticles (390 Oe) and the ϵ Co nanoparticles (1400 Oe; Figure 9A). Although, as predicted, the larger size particles when they are less than the critical size of about 20 nm have higher coercivities, the 3.5 nm hcp Co nanoparticles have a larger coercivity than 3.9 nm fcc Co and 4.7 nm ϵ Co. These results are similar to those obtained by Sun and Murray.[12] The ϵ Co nanoparticles also have a lower saturation field (H_s, 12 500 Oe) compared to the hcp Co (29 800 Oe) and that of the fcc Co (22 500 Oe), indicating that ϵ Co nanoparticles are softer magnetic materials than hcp Co, as seen by consideration of their coercivities.[12,44]

It is pertinent to mention that for the hcp Co samples the M versus H data present some unique features. Inspection of the data at $T = 300$ K shows an anomalous 11% decrease in M ($H = 5$ T) at the close of the cycle, compared to the corresponding value of M at the start of the cycle. In addition, the data at 10 K shows a 44 (emu/g) jump in the magnetization at $H = 0$ at the start of the M versus H cycle. The first of these anomalies may be due to improper packing of the sample; that is, the powder may have moved as the magnetic field is increased if the cotton plug is not packed in such a way as to keep it stationary. The effect of this would show up as the curve not retracing itself due to particle movement and corresponding spin reorientation in relation to the easy magnetization axis. The second anomaly may be due to a residual magnetic field if the degaussing procedure, described in the experimental procedure, had inadvertently not been done before inserting the sample into the sample space. The resulting residual magnetic field in the sample chamber would cause an offset in the magnetization on the hysteresis curve. On the other hand, it is possible that the hcp Co sample may be more susceptible to the measurement procedure (application the 100 G magnetic field used in the M vs T measurement prior to measuring M vs H, thus introducing a remnant effect in the samples) than the other structures. Although the source(s) of the anomalies is (are) not clear at the present time we have presented the hcp Co sample data in Table 1 because they may suggest a trend that has importance in an overall comparison of the samples. The extracted values, for the hcp Co sample, that are based on the $H = +5$ T going to the $H = -5$ T portion of the hysteresis curve are included in Table 1.

Even though a detailed mechanistic investigation is required to understand the reasons for phase control in this synthesis, a plausible explanation based on differences in collision energies and crystal structure transformation under different conditions can be proposed (Figure 10). Particle growth appears to be suppressed effectively by the quenching process, which leads to a rapid removal of free atoms from the solution. This indicates also that interparticle agglomeration is negligible. In contrast to that, in the unquenched sample particle, growth is observed as a separate step.

It is worth noting that despite significantly different retention times in the reactor for high flow rate (3.4 s) and low flow rate conditions (36 s), the size of the particles (3.9 ± 0.9 nm versus 3.5 ± 0.7 nm) is virtually independent of the flow rate for the immediately quenched particles. Further growth of the particles appears to take place outside of the reactor if the reaction is not quenched immediately. This indicates that after a quick first step in nanoparticle formation, further increase in particle size occurs on a much slower

(43) Margeat, O.; Amiens, C.; Chaudret, B.; Lecante, P.; Benfield, R. E. *Chem. Mater.* **2005**, *17* (1), 107.

(44) Yang, H. T.; Su, Y. K.; Shen, C. M.; Yang, T. Z.; Gao, H. J. *Surf. Interface Anal.* **2004**, *36* (2), 155.

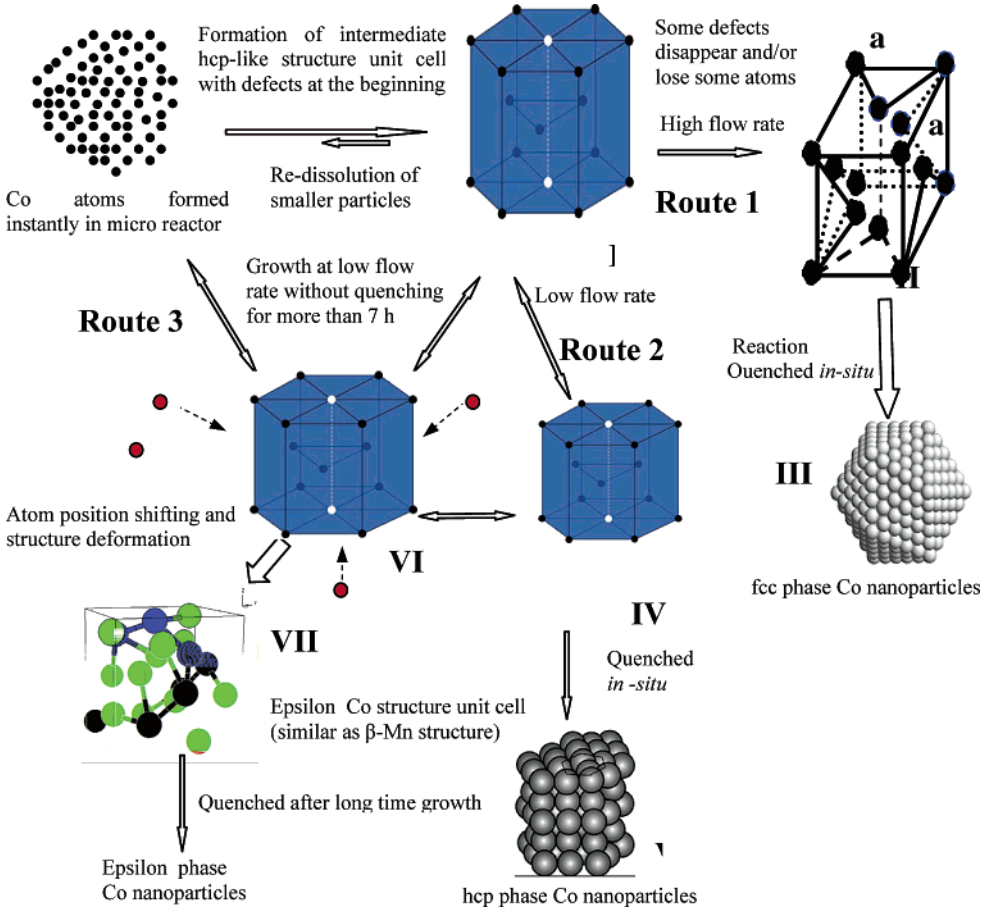

Figure 10. Schematic representation of the proposed formation route for the fcc, hcp, and ϵ Co nanoparticles using a microfluidic reactor.

time scale, and potentially this may be interpreted in terms of nucleation and growth, respectively. It is also likely that one could separate the reaction stages into a nucleation stage or growth stage by adjusting the flow rate and the reaction channel length and by adding the reagents at predetermined (based on modeling studies) positions into the channels. However, additional experiments are needed to provide a more detailed analysis.

The three different crystal structures of cobalt nanoparticles are likely to be obtained through kinetic control, as they are three nearly isoenergetic crystal structures (the calculated $\Delta G_f^{f\rightarrow h}$ from 3.9 nm fcc phase Co to 3.5 nm hcp phase Co is about 0.78 kJ/mol).[14,17,44] When the flow rate increases from 0.08 mL/min to 0.9 mL/min, the kinetic energy of the fluids increases by a factor of 115 assuming a laminar flow. Despite this increase in kinetic energy, the corresponding particle energies remain too small to explain the phase transformation when considering laminar flow. However, in the reactor we deliberately created turbulence, by designing micromixers within the reactor chip [see our publication (ref 9)], which is expected to increase further by higher flow because of the dependence of the Reynolds number on the particle velocity. Consequently, a more turbulent flow of the fluid in the reactor is likely to lead to higher kinetic energy of the individual particles (which is difficult to quantify unless one resorts to complex mathematical modeling taking into consideration design of the micromixer and its position within the microfluidic channels) than anticipated for the fluid under laminar flow resulting in the formation of fcc phase Co nanoparticles (see Figure 10, route 1). This increase in kinetic energy is likely to produce hcp-like unit cells of single crystals heavily laced with stacking faults, thereby helping to reduce the kinetic barrier to zero for their transformation to the fcc phase.[12,15,45] A comparable situation is encountered in the phase transformation from hcp to fcc Co obtained by strain at high mill intensity during ball milling.[17] In contrast to that, at a low flow rate the intermediate hcp-like unit cells, with less stacking faults, will have enough time to form a stable hcp structure unit cell (route 2, structures IV and V in Figure 10). The kinetic barrier is likely to prevent the phase transformation from hcp to fcc because the reaction is conducted at room temperature (20 ± 2 °C) and the calculated heat of the reaction was found to be negligible. Hence, the flow-induced increase in kinetic energy should be the dominant factor rather than an increase in thermal energy. This is also supported by our observation that the fcc structure is formed at a higher temperature (35−40 °C) when using the microfluidic reactor or when the reaction was conducted under ultrasonication in a conventional batch process.[25]

In addition, shear stress is more likely pronounced at lower flow rates because of the "chip-effect" from the channel wall.[46] This probably affects the interaction between the surfactant and the metallic cores. Ostwald ripening and/or isothermal recrystallization may occur if free Co atoms

(45) Lewis, W. F. *J. Appl. Phys.* **1978**, *49* (4), 2470.
(46) Monica, B.; Oosterbroek, R. E.; Verboom, W.; Goedbloed M. H.; van den Berg, A.; Reinhoudt, D. N. *Chem. Commun.* **2003**, 1924.

remain available in the solution, that is, if the nanoparticle solution is not quenched immediately. As a consequence, the hcp-like intermediate unit cells or the hcp Co unit cell can absorb six more isolated Co atoms from the dissolved small particles to form unit cells with 20 Co atoms (structure VI) finally growing up to the 4.7 nm ϵ Co structure (structure VII),[12,14,46] near to the critical size of 5.1 nm of spherical encapsulated Co nanoparticles according to the Gibb's free energy.[14] The formation of ϵ Co nanoparticles at room temperature by formation of bigger particles at the expense of the smaller ones (route 3) can also be envisaged.[47] Detailed mechanistic investigations are in progress.

4. Conclusion

We have developed a phase-controlled synthesis of cobalt nanoparticles using a polymeric microfluidic reactor through variation of experimental conditions such as flow rates, growth time, and quenching procedure. It was shown that Co nanoparticles with mainly fcc structure were formed at reaction conditions with a high kinetics energy level (e.g., high flow rate). At reaction conditions with a low kinetics energy level (e.g., low flow rate) and short growth time, Co nanoparticles with mainly hcp structures were favored. When the Co nanoparticles formed at the low kinetics level grew for a longer time, the crystal structure of Co nanoparticles shifted to the metastable phase, or ϵ structure. This result suggests a potential application to use microfluidic reactors to obtain nanoparticles with different structures by precisely controlling the reaction kinetics, which will affect the properties (e.g., magnetic properties) of the as-synthesized nanoparticles. The magnetic characterization showed reduced magnetic properties compared with properties of bulk Co. This is attributed to possible remnants of the surfactant used in the fabrication process rather than to a size effect.

Acknowledgment. This work was supported by grants from NSF-EPSCoR (Grant NSF/LEQSF (2001-04) RII-03) through Louisiana Board of Regents and DARPA biomagnetics project (Grant HR0011-04-C-0068). The authors thank Dr. J. Jiang and Prof. Meletis of the Mechanical Engineering Department of LSU for the use of the transmission electron microscope.

CM052811D

(47) Sohnel, O.; Garside, J. *Precipitation-Basic Principles and Industrial Applications*; Butterworth-Heinemann, Ltd.: Oxford, 1992.